Research Square

Preprints are preliminary reports that have not undergone peer review.
They should not be considered conclusive, used to inform clinical practice,
or referenced by the media as validated information.

Critical Crossings and Quantum Friction in a Finite-Time XY-Chain Otto Engine

Geronimo Allan Jerome Acosta

gacosta@nip.upd.edu.ph

University of the Philippines Diliman

Cristine Villagonzalo

University of the Philippines Diliman

Article

Keywords:

Posted Date: November 11th, 2026

DOI: https://doi.org/10.21203/rs.3.rs-11275667/v1

License: This work is licensed under a Creative Commons Attribution 4.0 International License.
Read Full License

Additional Declarations: No competing interests reported.

Critical Crossings and Quantum Friction in a Finite-Time XY-Chain Otto Engine

Geronimo Allan Jerome G. Acosta[1, 2, *] **and Cristine D. Villagonzalo**[2]

[1]National Institute of Physics, University of the Philippines Diliman, Quezon City, 1101, Philippines
[2]College of Sciences, Palawan State University, Puerto Princesa City, Palawan, 5300, Philippines
[*]gacosta@nip.upd.edu.ph

ABSTRACT

We investigate the finite-time performance of a quantum Otto engine with a transverse-field anisotropic XY spin chain as its working medium. By decomposing the chain into independent momentum sectors, we calculate mode-resolved transition probabilities during linear transverse-field ramps. We determine the resulting excitation density, work, heat, efficiency, and power for driving protocols in which the transverse field is varied linearly between prescribed endpoints during the two unitary strokes, while the anisotropy remains fixed. Protocols crossing one or both quantum critical points exhibit Kibble–Zurek scaling, $n_{\mathrm{ex}} \sim \tau^{-1/2}$, whereas protocols that maintain a nonzero energy gap throughout the ramps exhibit the faster decay $n_{\mathrm{ex}} \sim \tau^{-2}$, where τ is the duration of each ramp. The work separates into an endpoint-dependent adiabatic contribution and a nonnegative contribution associated with quantum friction. At short driving times, quantum friction can exceed the adiabatic work output and prevent heat-engine operation. At long driving times, the thermodynamic quantities approach adiabatic values determined by the endpoint spectra and thermal population imbalances. Increasing anisotropy suppresses excitations and hastens the approach to the adiabatic limit. These results distinguish endpoint thermodynamics from critical-crossing dynamics and clarify their roles in finite-time engine performance.

Introduction

Quantum heat engines are theoretical and experimental devices that convert heat into useful work using quantum systems as working media[1–3]. Unlike classical heat engines, quantum heat engines operate using discrete energy levels and exhibit phenomena such as coherence, entanglement, and non-equilibrium excitations. These systems have attracted significant attention due to their relevance in thermal management of nanoscale metrology and quantum technologies[3–8].

Recent developments in quantum computing and quantum information processing have intensified interest in understanding thermodynamic processes[9–11] at the quantum scale. In particular, spin-chain systems provide a useful framework for studying the relationship between many-body quantum dynamics and thermodynamic performance[3,12,13]. Among these, the transverse-field XY spin-$1/2$ chain is especially important because it exhibits quantum phase transitions and allows exact diagonalization through Jordan–Wigner and Bogoliubov transformations[14–16].

When a quantum system is driven across a critical point at finite speed, the closing of the energy gap generates nonadiabatic excitations[17–20]. These excitations contribute to irreversible entropy production and reduce the efficiency of quantum thermal machines[19,20]. At the same time, critical regions may also enhance thermodynamic response due to increased energy fluctuations[21,22]. Understanding these competing effects is therefore important for determining whether quantum criticality can improve the operation of finite-time quantum heat engines.

In this work, we investigate a finite-time quantum Otto engine using the transverse-field anisotropic XY spin-$1/2$ chain as the working medium. By decomposing the chain into independent momentum sectors, we calculate the exact finite-time transition probability of each effective two-level mode during linear ramps of the transverse field. We compare driving protocols in which the transverse field is varied linearly between prescribed endpoints during the two unitary strokes, while the anisotropy remains fixed. These protocols either remain within a gapped phase, where the energy gap between the ground state and the lowest excited state stays nonzero throughout the ramp, or cross one or both quantum critical points, where this gap closes in the thermodynamic limit. For each protocol, we determine the resulting excitation density, work output, heat exchange, efficiency, and power. Particular attention is given to the asymptotic dependence on the driving time, the role of the anisotropy parameter, and the separation of the total work into adiabatic and nonadiabatic contributions. This analysis allows us to distinguish two effects in literature[19,22,23] that are often combined and indistinguishable from each other. These are (1) the endpoint spectra and reservoir temperatures determine the adiabatic thermodynamic values, whereas (2) the critical points encountered along the driving path determine the magnitude and decay rate of the finite-time corrections.

Quantum Otto Engine

Working Medium

The working medium is modeled using the one-dimensional transverse-field XY spin-$1/2$ chain with Hamiltonian given as,

$$H(h,\gamma) = -\sum_{j=1}^{N}\left[\frac{1+\gamma}{2}\sigma_j^x\sigma_{j+1}^x + \frac{1-\gamma}{2}\sigma_j^y\sigma_{j+1}^y + h\,\sigma_j^z\right], \tag{1}$$

where $h = \frac{g}{J}$ denotes the dimensionless transverse field, with g the strength of the transverse magnetic field and J the nearest-neighbor exchange coupling constant. The parameter γ is the anisotropy parameter, and σ_j^α $(\alpha = x,y,z)$ denotes the Pauli matrix acting on the j^{th} spin. Periodic boundary conditions are assumed, such that $\sigma_{N+1}^\alpha = \sigma_1^\alpha$.

The Hamiltonian is diagonalized into independent quasiparticle modes, allowing the finite-time dynamics to be analyzed as a collection of independent driven two-level systems given by,

$$H = \sum_{k>0} E_k(h,\gamma)\left(\eta_k^\dagger\eta_k - \frac{1}{2}\right), \tag{2}$$

where k denotes the crystal momentum (quasimomentum) associated with the fermionic modes. For a chain of N spins with periodic boundary conditions, k takes discrete values in the first Brillouin zone, and the summation over $k>0$ counts one representative from each $(k,-k)$ pair. Here, η_k are Bogoliubov quasiparticle operators, and the corresponding dispersion relation is

$$E_k(h,\gamma) = 2\sqrt{(h-\cos k)^2 + \gamma^2\sin^2 k}. \tag{3}$$

Thermodynamic Cycle

The quantum Otto cycle operates between a cold and hot reservoir at inverse temperatures β_c and β_h, respectively. The inverse temperatures are defined as $\beta = \frac{1}{k_B T}$ with T the temperature of the reservoir. Moreover, the fields h_c and h_h are fixed transverse-field values during thermalization with the cold and hot reservoirs, respectively. The quantum Otto cycle consists of four strokes:

1. **Cold thermalization (A):** The system thermalizes with a cold bath at inverse temperature β_c, reaching the Gibbs state of $H_c = H(h_c,\gamma)$ with energy E_A.
2. **Forward unitary driving (A→B):** The field is ramped from h_c to h_h according to Eq. (4). The energy at the end of the stroke is E_B.
3. **Hot thermalization (C):** The system thermalizes with a hot bath at inverse temperature β_h, reaching the Gibbs state of $H_h = H(h_h,\gamma)$ with energy E_C.
4. **Reverse unitary driving (C→D):** The field is ramped back from h_h to h_c, yielding an energy E_D.

The unitary strokes of the Otto cycle are implemented by linearly ramping the transverse field while keeping the anisotropy fixed,

$$h(t) = h_i + \frac{h_f - h_i}{\tau}t, \qquad \gamma(t) = \gamma, \qquad 0 \le t \le \tau, \tag{4}$$

where τ is the ramp duration, and h_i and h_f are the initial and final transverse fields of each unitary stroke. For the forward stroke, $(h_i,h_f) = (h_c,h_h)$, whereas for the reverse stroke, $(h_i,h_f) = (h_h,h_c)$. We assume complete thermalization during each thermal stroke, so that the working medium reaches the Gibbs state corresponding to the reservoir temperature and the fixed transverse field, h_c or h_h, before the next unitary stroke.

Dynamics and Working Regimes

For each $(k,-k)$ sector, the time-dependent Hamiltonian is written as

$$H_k(t) = 2\left[(h(t)-\cos k)\,\sigma_z + \gamma\sin k\,\sigma_x\right]. \tag{5}$$

The initial Gibbs state of each mode is diagonal in the instantaneous eigenbasis of the initial Hamiltonian. If the initial inverse temperature is β, the excited-state occupation is

$$n_k^{\text{in}} = \frac{1}{e^{\beta E_k(h_i)}+1}. \tag{6}$$

The finite-time unitary dynamics are obtained from the time-dependent Schrödinger equation

$$i\frac{d}{dt}|\psi_k(t)\rangle = H_k(t)|\psi_k(t)\rangle. \tag{7}$$

The exact formal solution is

$$|\psi_k(\tau)\rangle = \mathscr{T}\exp\left[-i\int_0^\tau H_k(t)\,dt\right]|\psi_k(0)\rangle, \tag{8}$$

where $\mathscr{T}$ denotes time ordering. The energy of each mode at the end of the ramp is evaluated from the expectation value of the final Hamiltonian,

$$e_k^{\text{out}} = \text{Tr}\big[\rho_k(\tau)H_k(h_f)\big]. \tag{9}$$

Finally, the total energy density is obtained by integrating over all independent momentum sectors in the thermodynamic limit:

$$\mathscr{E} = \frac{1}{2\pi}\int_0^\pi e_k\,dk. \tag{10}$$

The four points of the Otto cycle are then computed as follows. At point **A**, the system is in thermal equilibrium with the cold bath,

$$E_A = \mathscr{E}_{\text{th}}(\beta_c, h_c, \gamma). \tag{11}$$

After the first unitary stroke $h_c \to h_h$, the energy is

$$E_B = \mathscr{E}_{\text{unitary}}(\beta_c, h_c \to h_h, \gamma, \tau). \tag{12}$$

The hot isochore is assumed to produce complete thermalization, so

$$E_C = \mathscr{E}_{\text{th}}(\beta_h, h_h, \gamma). \tag{13}$$

After the reverse unitary stroke $h_h \to h_c$, the energy is

$$E_D = \mathscr{E}_{\text{unitary}}(\beta_h, h_h \to h_c, \gamma, \tau). \tag{14}$$

The heat exchanged with the hot and cold reservoirs is

$$Q_h = E_C - E_B, \qquad Q_c = E_A - E_D. \tag{15}$$

The work performed during the two unitary strokes is

$$W_2 = E_B - E_A, \qquad W_4 = E_D - E_C, \tag{16}$$

and the net work is

$$W = W_2 + W_4. \tag{17}$$

With the sign convention used here, $W < 0$ corresponds to net work output by the engine. The operating regimes are classified according to the signs of W, Q_h, and Q_c:

$$\text{Heat engine:} \quad W<0, \quad Q_h>0, \quad Q_c<0, \tag{18}$$

$$\text{Refrigerator:} \quad W>0, \quad Q_h<0, \quad Q_c>0, \tag{19}$$

$$\text{Heater/Dissipator:} \quad W>0, \quad Q_h>0, \quad Q_c<0, \tag{20}$$

$$\text{Accelerator:} \quad W<0, \quad Q_h<0, \quad Q_c>0. \tag{21}$$

Parameter points that do not satisfy any of these set conditions are grouped into an additional "other" category.

Performance measures

The performance in the heat-engine regime is quantified using the efficiency and power. Due to the assumption of complete thermalization and disregarding the thermalization time, the power measured in this study is the work per driving time. The efficiency is defined as,

$$\eta = -\frac{W}{Q_h}, \tag{22}$$

while the power is calculated as,

$$P_d = -\frac{W}{2\tau}. \tag{23}$$

Moreover, the exact finite-time transition probability for each mode-k was numerically calculated using the following results,

$$p_k = \left|\langle e_f|F(t_f)F^{-1}(t_i)|g_i\rangle\right|^2, \tag{24}$$

where F is the fundamental matrix of the two-level system corresponding to each k-mode, g_i is the instantaneous ground state at the start of driving at t_i, and e_f is the instantaneous excited state at the end of driving at t_f. The excitation density was calculated by summing the excitation probability over all k-modes, given by the following integral,

$$n_{ex}(\tau) = \frac{1}{\pi}\int_0^{\pi} p_k(\tau)dk. \tag{25}$$

Numerical methods

Calculations were implemented in Python 3.13.5 using NumPy 2.3.1, mpmath 1.3.0, and Matplotlib 3.10.3. For each momentum sector, the finite-time propagator $U_k(\tau,0) = F_k(\tau)F_k^{-1}(0)$ was evaluated using parabolic-cylinder functions. Transition probabilities were obtained by projecting the evolved initial ground state onto the final instantaneous excited state.

Excitation densities and thermodynamic quantities were integrated over uniformly sampled momenta using the composite trapezoidal rule. The endpoints $k = 0, \pi$ were excluded because the chosen fundamental-matrix representation becomes singular there. Driving durations were sampled logarithmically. Complete thermalization and mutually time-reversed unitary strokes were assumed. Efficiency and driving-time power, $P_d = W_{\text{out}}/(2\tau)$, were reported only in the heat-engine regime, with thermalization times excluded.

Power-law exponents were obtained by unweighted least-squares fits of $\log_{10} n_{\text{ex}}$ against $\log_{10}\tau$, using finite, positive excitation densities.

Results and Discussion

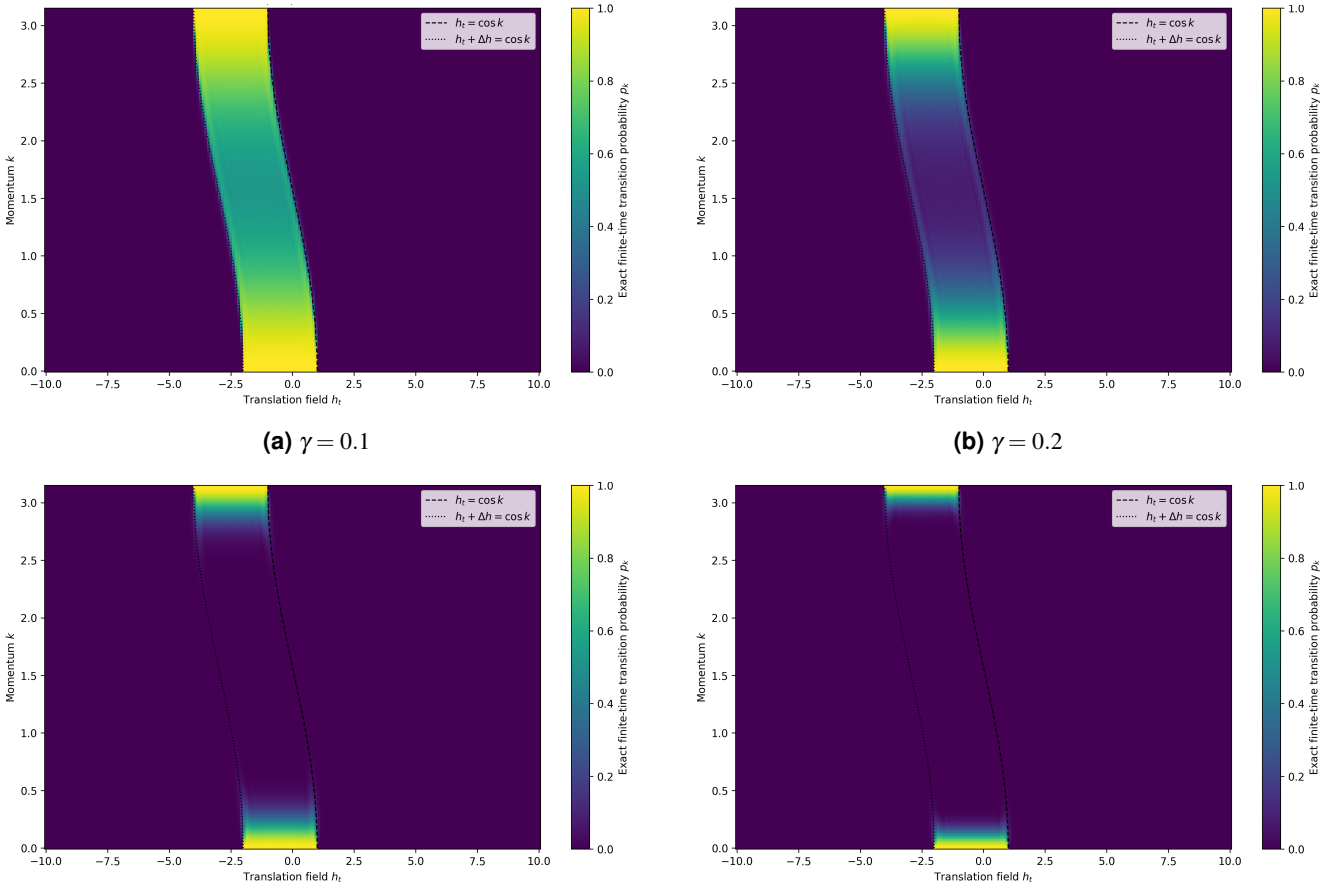
Exact Finite Time Transition Probability

Figure 1 shows the heatmap of the exact finite time probability $p_k(\gamma, \Delta h, \tau, h_t)$ for different modes, k, and driving window defined by h_t, with $h_c = h_t$ and $h_h = h_t + \Delta h$. The heatmap shows a vertical strip with inner part containing the high p_k regions while the outer regions correspond to low or near zero p_k values. The strip is bounded from the top by $k = \pi$, from below by $k = 0$, and from the left and right by the curves corresponding to the functions $h_t = \cos(k)$ and $h_t = \cos(k) - \Delta h$ with Δh dictating the strip width. The density of high value p_k's inside the strip decreases with the magnitude of γ while maintaining near unity value near the critical k-modes, $k = -\pi, 0, +\pi$. The behavior of p_k can be attributed to two factors: from the avoided crossings when the driving protocol crosses the minimum gap between the two states of the Hamiltonian H_k and to the proximity of the protocol to the critical points $h = \pm 1$ when the gap closes.

It is convenient to categorize the different protocol regions using the number of avoided critical points during the driving.

1. **No crossing.** The driving protocol does not cross either critical point, $h = \pm 1$. This occurs when both h_c and h_h lie within the same phase region:

$$h_c < h_h < -1, \qquad -1 < h_c < h_h < 1, \qquad \text{or} \qquad 1 < h_c < h_h.$$



(a) $\gamma = 0.1$ **(b)** $\gamma = 0.2$

(c) $\gamma = 0.5$ **(d)** $\gamma = 0.9$

Figure 1. Exact transition probability p_k versus momentum k and translation field $h_t = h_c$, for the indicated anisotropies, with $\Delta h = 3$ and $\tau = 30$. Dashed and dotted curves mark $h_t = \cos k$ and $h_t + \Delta h = \cos k$, respectively, bounding the mode-crossing region.

2. **Single-crossing.** The driving protocol crosses exactly one of the two critical points. Crossing $h = -1$ occurs when

$$h_c < -1 < h_h < 1,$$

while crossing $h = +1$ occurs when

$$-1 < h_c < 1 < h_h.$$

3. **Double-crossing.** The driving protocol crosses both critical points, $h = -1$ and $h = +1$, during the same stroke. This occurs when

$$h_c < -1 < 1 < h_h.$$

Figure 1 parameters were chosen to demonstrate the double crossing protocols and to highlight the effects of γ.

The different protocols correspond to different cross sections of the p_k heat map, as shown in Figure 2. In the outer phases (blue curves), protocols with no crossings yield near-zero transition probabilities for all modes. Single-crossing protocols (orange line) correspond to cross sections in which p_k increases toward unity near the critical modes $k = \pm\pi$. For $\Delta h < 2$, the central-phase protocol has no critical crossings, and the corresponding cross section (green-left) cuts through the middle of the strip without passing through either end. This cross section is characterized by a central region of modes with nonzero transition probabilities. In contrast, for $\Delta h > 2$, the central-phase protocols involve double crossings, and the corresponding cross section (green-right) passes through both ends of the strip. Here, p_k is near unity close to the critical modes and decreases toward the central modes.

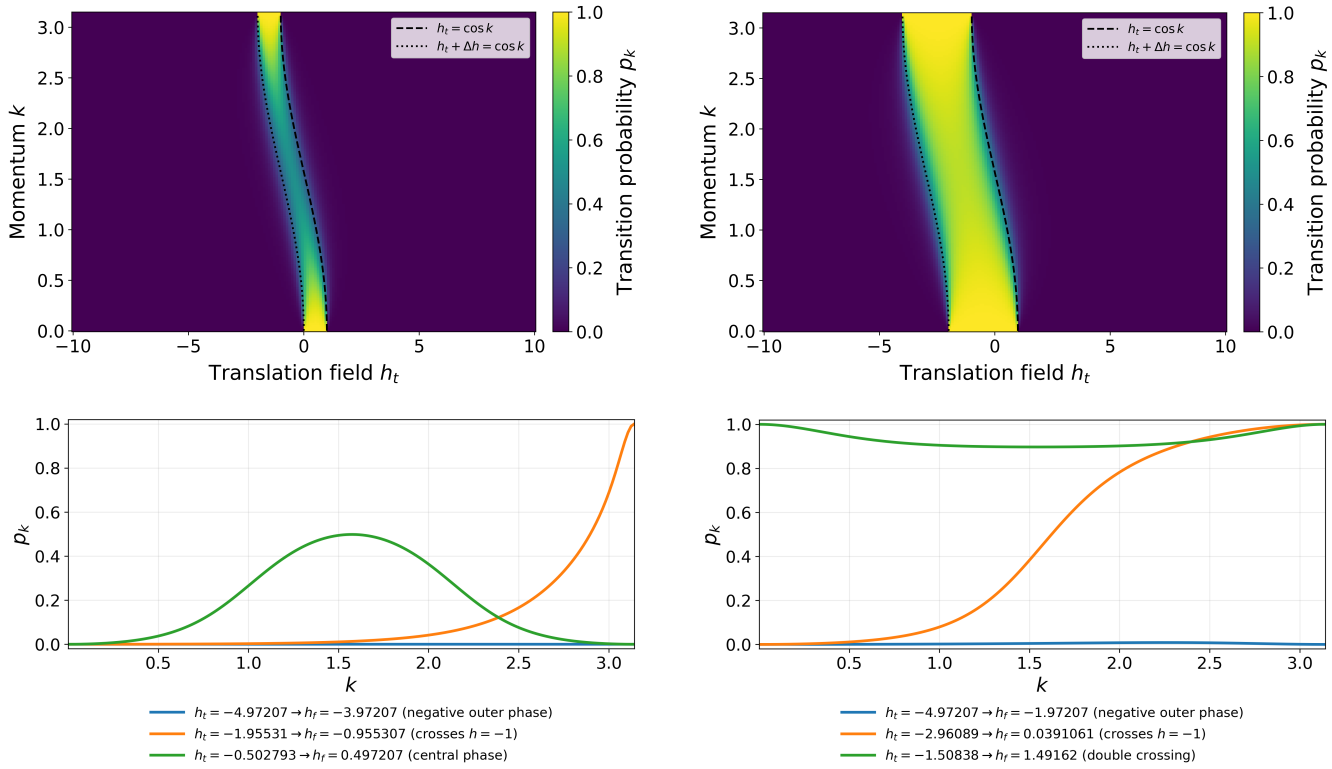
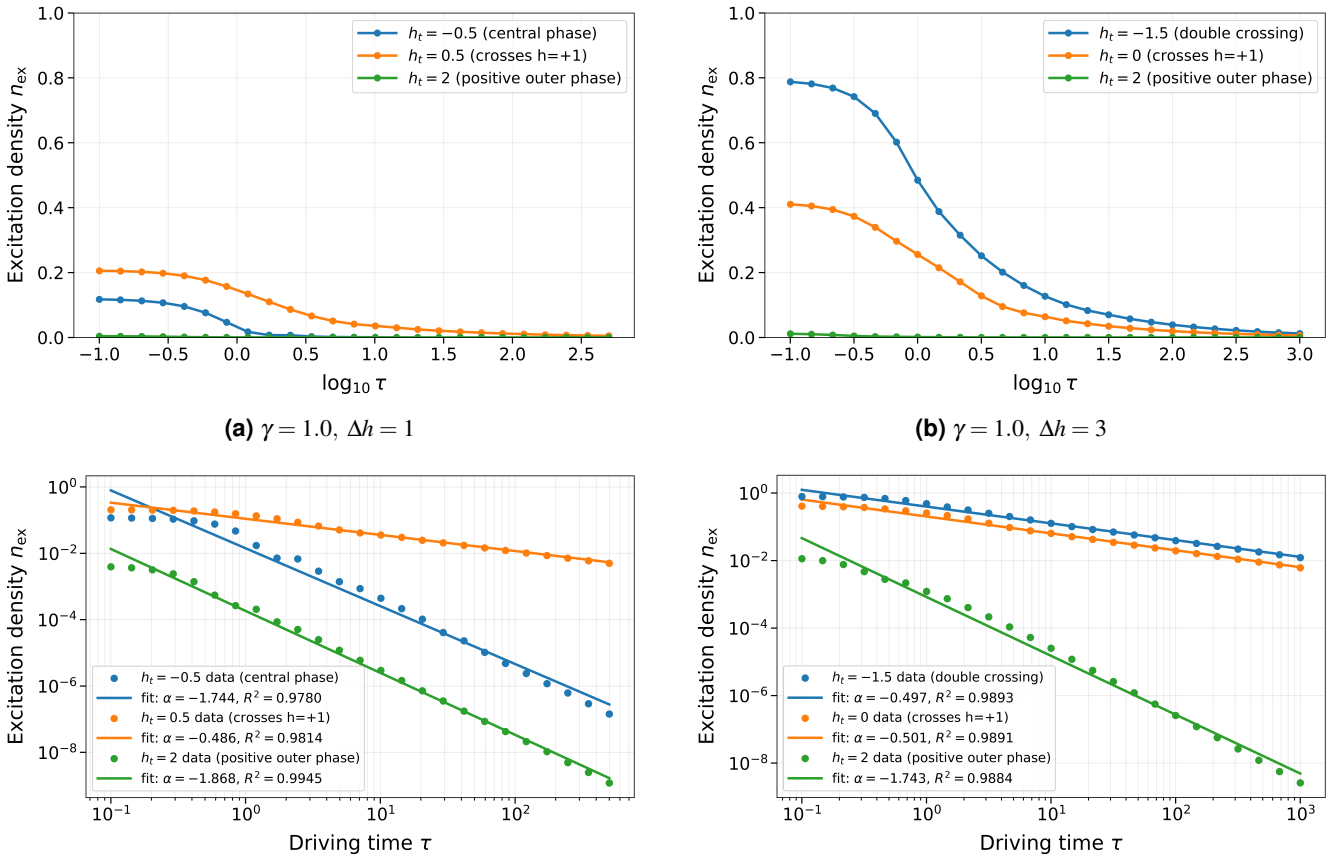


Figure 2. Transition-probability maps (top) and representative momentum cross sections (bottom) for $\gamma = 0.5$, $\tau = 0.1$, and $\Delta h = 1$ (left) or 3 (right). Boundary curves are defined in Fig. 1. Protocol endpoints are given in the legends.

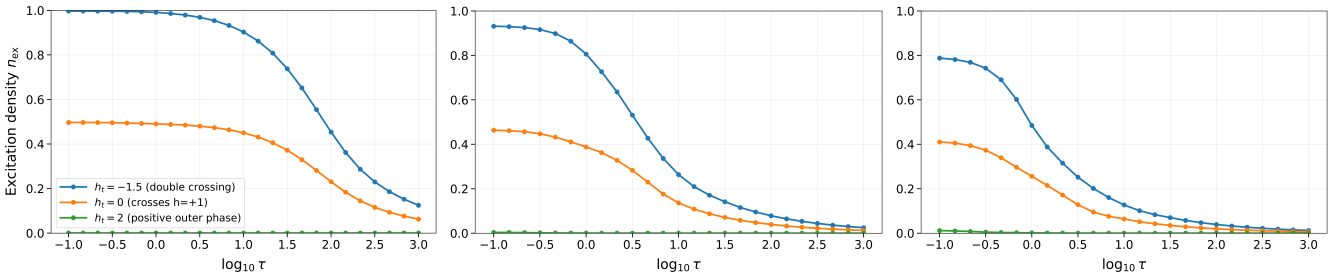
Figure 3 presents the plots of excitation probability density with the driving time τ for cases $\Delta h = 1 < 2$ and $\Delta h = 3 > 2$ where the central phases corresponds to no crossing and double-crossing, respectively. The log-log plot shows a Kibble-Zurek power law scaling $n_{ex} \sim \tau^{-\frac{1}{2}}$ for single and double crossings and a power law scaling of $n_{ex} \sim \tau^{-2}$ for protocols without crossing (outer phases). Additionally, the excitation density generally increases with the number of critical crossings. Moreover, Figure 4 shows that increasing γ suppresses the excitation density and reduces the driving time required to approach the adiabatic regime, where transition probabilities become negligible.



(a) $\gamma = 1.0,\ \Delta h = 1$ **(b)** $\gamma = 1.0,\ \Delta h = 3$

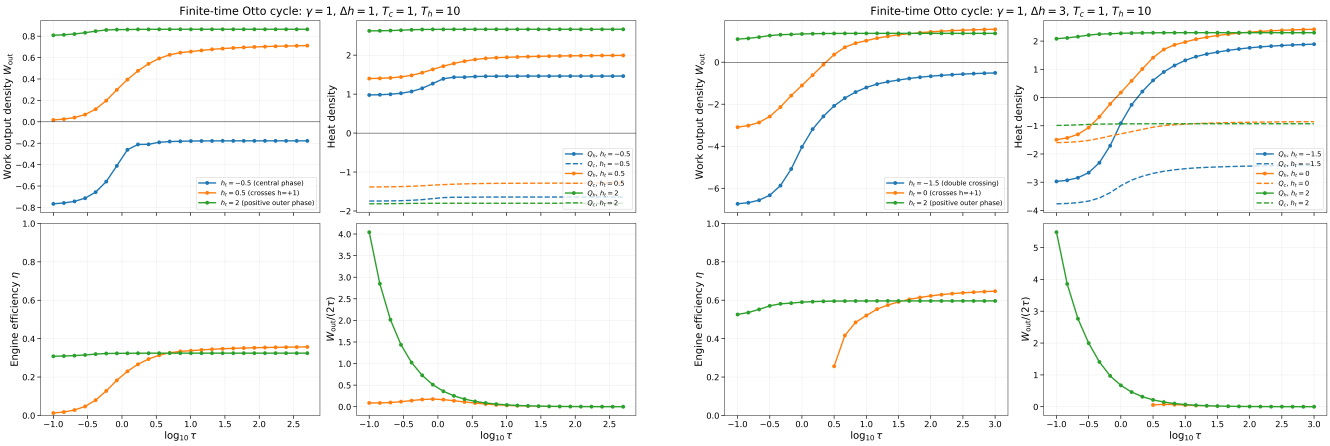
(c) $\gamma = 1.0,\ \Delta h = 1$ **(d)** $\gamma = 1.0,\ \Delta h = 3$

Figure 3. Excitation density versus driving time for $\gamma = 1$, with $\Delta h = 1$ (left) and 3 (right). Upper panels show the full time range. Lower panels show large-τ power-law fits, with exponents given in the legends.



(a) $\gamma = 0.1,\ \Delta h = 3$ **(b)** $\gamma = 0.5,\ \Delta h = 3$ **(c)** $\gamma = 1.0,\ \Delta h = 3$

Figure 4. Excitation density versus driving time for the indicated anisotropies and $\Delta h = 3$. Protocols $h_t = -1.5$, 0, and 2 correspond to double, single, and no critical crossings, respectively.



(a) $\gamma = 1.0,\ \Delta h = 1$ **(b)** $\gamma = 1.0,\ \Delta h = 3$

Figure 5. Otto-cycle thermodynamics versus driving time for $\gamma = 1$, $T_c = 1$, $T_h = 10$, and (a) $\Delta h = 1$ or (b) 3. Each panel shows work output (upper left), heat exchange (upper right), efficiency (lower left), and power $P = W_{\text{out}}/(2\tau)$ (lower right), excluding thermalization times. Solid and dashed heat curves denote Q_h and Q_c. Efficiency and power are shown only where $W_{\text{out}} > 0$, $Q_h > 0$, and $Q_c < 0$.

For compression and expansion protocols that are exact time reversals of one another, the corresponding transition probabilities are equal:

$$p_k^{c\to h} = p_k^{h\to c} \equiv p_k(\tau), \tag{26}$$

where the dependence on the duration τ of each unitary stroke has been written explicitly. The total work performed on the k-mode during one complete cycle can then be decomposed into adiabatic and nonadiabatic contributions:

$$W_{\text{total},k}(\tau) = W_{\text{ad},k} + W_{\text{fric},k}(\tau). \tag{27}$$

The adiabatic contribution is

$$W_{\text{ad},k} = \left(E_{k,c} - E_{k,h}\right)\left(r_{k,c} - r_{k,h}\right) \tag{28}$$

where

$$r_{k,c} = \tanh\left(\beta_c E_{k,c}\right), \qquad r_{k,h} = \tanh\left(\beta_h E_{k,h}\right) \tag{29}$$

are the thermal population-difference factors at the cold and hot points of the cycle. Here, $\alpha \in c,h$ labels the cold and hot thermalization points, respectively; $E_{k,\alpha}$ is the corresponding mode energy, and $r_{k,\alpha}$ is the thermal population-difference factor. The nonadiabatic contribution is

$$W_{\text{fric},k}(\tau) = 2p_k(\tau)\left(E_{k,h}r_{k,c} + E_{k,c}r_{k,h}\right). \tag{30}$$

Because $p_k(\tau) \geq 0$, $E_{k,\alpha} \geq 0$, and $r_{k,\alpha} \geq 0$, it follows that

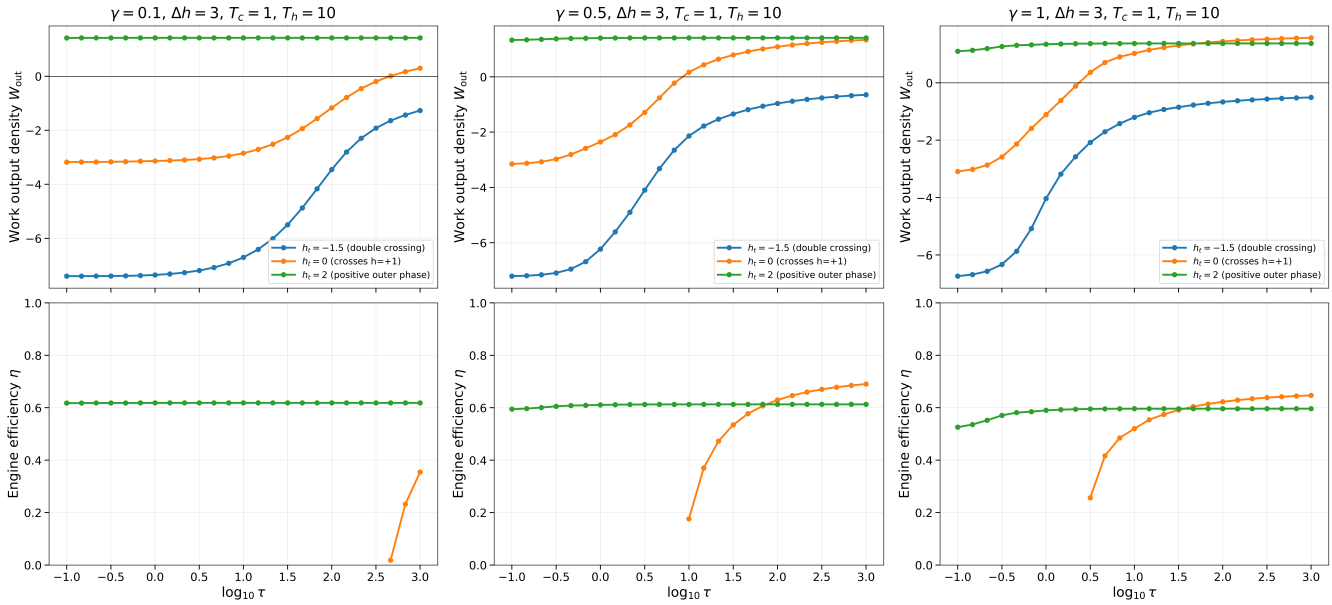
$$W_{\text{fric},k}(\tau) \geq 0. \tag{31}$$

Thus, nonadiabatic transitions always increase the work performed on the working medium. With the present sign convention, the useful work delivered by the k-mode is

$$W_{\text{out},k}(\tau) = -W_{\text{total},k}(\tau) = W_{\text{out},k}^{\text{ad}} - W_{\text{fric},k}(\tau), \tag{32}$$

where

$$W_{\text{out},k}^{\text{ad}} = -W_{\text{ad},k} = \left(E_{k,h} - E_{k,c}\right)\left(r_{k,c} - r_{k,h}\right). \tag{33}$$



(a) $\gamma = 0.1,\ \Delta h = 3$ **(b)** $\gamma = 0.5,\ \Delta h = 3$ **(c)** $\gamma = 1.0,\ \Delta h = 3$

Figure 6. Work-output density (top) and heat-engine efficiency (bottom) versus driving time for the indicated anisotropies, with $\Delta h = 3$, $T_c = 1$, and $T_h = 10$. Protocols $h_t = -1.5$, 0, and 2 correspond to double, single, and no critical crossings, respectively. Efficiency is shown only in the heat-engine regime.

Equation (32) shows that nonadiabatic transitions reduce the useful work output. When the quantum-friction contribution exceeds the adiabatic work output, the cycle requires net work input and no longer operates as a heat engine.

Heat is exchanged only during the isochoric thermalization strokes. The heat absorbed by the k-mode from the hot reservoir is

$$Q_{h,k}(\tau) = E_{k,h}\left[(1-2p_k(\tau))\, r_{k,c} - r_{k,h}\right] \tag{34}$$

whereas the heat entering the working medium from the cold reservoir is

$$Q_{c,k}(\tau) = E_{k,c}\left[(1-2p_k(\tau))\, r_{k,h} - r_{k,c}\right]. \tag{35}$$

Under this convention, heat-engine operation requires $Q_h > 0$ and $Q_c < 0$. The positive quantity $-Q_c$ is the heat rejected to the cold reservoir.

The heat exchanges can also be separated into adiabatic and nonadiabatic contributions:

$$Q_{h,k}(\tau) = Q^{\mathrm{ad}}_{h,k} - Q^{\mathrm{na}}_{h,k}(\tau), \tag{36}$$
$$Q_{c,k}(\tau) = Q^{\mathrm{ad}}_{c,k} - Q^{\mathrm{na}}_{c,k}(\tau), \tag{37}$$

where

$$Q^{\mathrm{ad}}_{h,k} = E_{k,h}\left(r_{k,c} - r_{k,h}\right), \qquad Q^{\mathrm{na}}_{h,k}(\tau) = 2p_k(\tau)E_{k,h}r_{k,c}, \tag{38}$$
$$Q^{\mathrm{ad}}_{c,k} = -E_{k,c}\left(r_{k,c} - r_{k,h}\right), \qquad Q^{\mathrm{na}}_{c,k}(\tau) = 2p_k(\tau)E_{k,c}r_{k,h}. \tag{39}$$

The nonadiabatic heat corrections are nonnegative and satisfy

$$W_{\mathrm{fric},k}(\tau) = Q^{\mathrm{na}}_{h,k}(\tau) + Q^{\mathrm{na}}_{c,k}(\tau). \tag{40}$$

Consequently, the first law is satisfied separately for every momentum mode:

$$W_{\mathrm{total},k}(\tau) + Q_{h,k}(\tau) + Q_{c,k}(\tau) = 0. \tag{41}$$

Since the momentum sectors evolve independently, the total work and heat are obtained by summing over all dynamically active modes:

$$W_{\text{total}} = \sum_{k>0} W_{\text{total},k}, \qquad Q_h = \sum_{k>0} Q_{h,k}, \qquad Q_c = \sum_{k>0} Q_{c,k}. \tag{42}$$

The complete many-body system operates as a heat engine when

$$W_{\text{total}} < 0, \qquad Q_h > 0, \qquad Q_c < 0. \tag{43}$$

Individual momentum modes need not satisfy the same sign conditions. The operating regime of the complete system is determined by the total quantities after summation over all modes.

Within the heat-engine regime, the thermal efficiency is defined as the ratio of the total work output to the heat absorbed from the hot reservoir:

$$\eta(\tau) = \frac{W_{\text{out}}(\tau)}{Q_h(\tau)} = -\frac{\sum_{k>0} W_{\text{total},k}(\tau)}{\sum_{k>0} Q_{h,k}(\tau)} \tag{44}$$

Equivalently using equation (32),

$$\eta(\tau) = \frac{\sum_{k>0} W_{\text{out},k}(\tau)}{\sum_{k>0} Q_{h,k}(\tau)}. \tag{45}$$

Using the many-body first law,

$$W_{\text{total}} + Q_h + Q_c = 0, \tag{46}$$

the efficiency may also be written as

$$\eta(\tau) = 1 + \frac{\sum_{k>0} Q_{c,k}(\tau)}{\sum_{k>0} Q_{h,k}(\tau)}. \tag{47}$$

In the adiabatic limit, $p_k(\tau) \to 0$, all nonadiabatic contributions vanish:

$$W_{\text{fric},k} \to 0, \qquad Q^{\text{na}}_{h,k} \to 0, \qquad Q^{\text{na}}_{c,k} \to 0. \tag{48}$$

The efficiency therefore approaches

$$\eta_{\text{ad}} = \frac{\sum_{k>0} \left(E_{k,h} - E_{k,c}\right)\left(r_{k,c} - r_{k,h}\right)}{\sum_{k>0} E_{k,h}\left(r_{k,c} - r_{k,h}\right)}. \tag{49}$$

The different adiabatic-limit values obtained for the protocols in Fig. 5 are determined by their endpoint spectra $E_{k,c}$ and $E_{k,h}$, together with the corresponding thermal population imbalance $r_{k,c} - r_{k,h}$. Although the protocols have the same field width Δh, changing h_c translates both endpoints across the phase diagram. This changes both the spectral deformation $E_{k,h} - E_{k,c}$ and the population imbalance available for work extraction. The higher efficiencies observed for the critical-crossing protocols therefore reflect their more favorable endpoint-dependent adiabatic values. The number of critical points crossed does not independently determine the strict adiabatic-limit value. Instead, the critical crossings primarily determine the magnitude and decay rate of the finite-time corrections through $p_k(\tau)$.

For a protocol that remains gapped, adiabatic perturbation theory gives $p_k(\tau) \sim \tau^{-2}$, so that the nonadiabatic thermodynamic corrections vanish as τ^{-2}. For a protocol crossing a quantum critical point, the Landau–Zener transition probability becomes concentrated around the critical momentum modes, resulting in the slower Kibble–Zurek scaling

$$W_{\text{fric}}(\tau),\ Q^{\text{na}}_h(\tau),\ Q^{\text{na}}_c(\tau) \sim \tau^{-1/2}. \tag{50}$$

Accordingly, all protocols approach endpoint-determined adiabatic values as $\tau \to \infty$, but critical-crossing protocols require longer driving times to reach their asymptotic plateaus. At short driving times, $p_k(\tau)$ remains nonzero, and the resulting nonadiabatic contribution may exceed the adiabatic work output, thereby suppressing heat-engine operation.

Conclusion

We investigated the finite-time operation of a quantum Otto engine using the transverse-field anisotropic XY spin-$1/2$ chain as the working medium. The integrability of the model allowed the many-body dynamics to be decomposed into independent momentum-resolved two-level systems. From their exact finite-time transition probabilities, we calculated the excitation density and the thermodynamic quantities of the complete Otto cycle, including the work output, heat exchange, efficiency, and power.

The excitation dynamics depend strongly on whether the driving trajectory remains gapped or crosses a quantum critical point. Protocols that remain within a gapped outer phase exhibit $n_{\mathrm{ex}} \sim \tau^{-2}$, consistent with adiabatic perturbation theory. In contrast, protocols crossing one or both critical points exhibit the slower Kibble–Zurek scaling $n_{\mathrm{ex}} \sim \tau^{-1/2}$. Double-crossing protocols generally generate more excitations than single-crossing protocols because nonadiabatic contributions arise near both critical momentum modes. Increasing the anisotropy parameter enlarges the avoided-crossing gaps, suppresses the transition probabilities, and reduces the driving time required to approach the adiabatic regime.

The thermodynamic analysis shows that the work performed on the working medium can be written as

$$W_{\mathrm{total}} = W_{\mathrm{ad}} + W_{\mathrm{fric}}, \tag{51}$$

where $W_{\mathrm{fric}} \geq 0$ is the nonadiabatic contribution associated with excitation production. At short driving times, the nonadiabatic contribution can exceed the adiabatic work output, reversing the sign of the net work so that the cycle requires work input rather than delivering work output and therefore no longer operates as a heat engine. Consequently, quantum friction always reduces the useful work output relative to its adiabatic value. For large τ, the nonadiabatic contribution vanishes as τ^{-2} for gapped protocols and as $\tau^{-1/2}$ for critical-crossing protocols. The work, heat, and efficiency then approach their adiabatic limits.

The different adiabatic plateaus obtained for the translated driving protocols are determined by the endpoint quasiparticle spectra and the thermal population imbalance between the cold and hot states. They are not determined solely by the number of critical points crossed. Critical crossings instead control the finite-time approach to these plateaus. This distinction is particularly important when assessing the thermodynamic role of quantum criticality: a critical trajectory may connect endpoints favorable for work extraction, but the same trajectory also generates excitations that reduce the output at finite driving time. Quantum criticality therefore introduces a competition between favorable endpoint thermodynamics and irreversible nonadiabatic losses.

The calculated power assumes complete thermalization and includes only the durations of the two unitary strokes. Consequently, its short-time behavior should be interpreted within this idealized cycle model and not as a prediction of unbounded physical power. Extensions of the present work could include finite thermalization times, incomplete system–bath relaxation, decoherence, optimized nonlinear driving protocols, and nonintegrable interactions. Such developments would help determine whether the finite-time advantages associated with critical working media persist under experimentally realistic conditions.

Data availability

The numerical datasets generated and analysed during the current study are available from the corresponding author upon reasonable request.

Code availability

The custom Python scripts used to calculate the finite-time transition probabilities, excitation densities, Otto-cycle thermodynamic quantities, and power-law fits, and to generate the figures, are available from the corresponding author upon reasonable request.

Acknowledgements

The authors acknowledge support from the National Institute of Physics, University of the Philippines Diliman. The authors also acknowledge discussions and consultations related to quantum thermodynamics and numerical simulations.

Author contributions

G.A.J.G.A. conceived the study, developed the theoretical framework, performed the numerical simulations, analyzed the results, and prepared the manuscript. C.D.V. supervised the research and reviewed the manuscript. All authors reviewed the final version of the manuscript.

Use of generative artificial intelligence

During manuscript preparation, the authors used ChatGPT (OpenAI) to assist with language editing, organization, and improving the clarity of selected passages. All generated text was reviewed, verified, and revised by the authors, who take full responsibility for the content of the manuscript.

Additional information

Competing interests: The authors declare no competing interests.

References

1. Alicki, R. The quantum open system as a model of the heat engine. *J. Phys. A: Math. Gen.* **12**, L103–L107, DOI: 10.1088/0305-4470/12/5/007 (1979).
2. Kosloff, R. A quantum-mechanical open system as a model of a heat engine. *The J. Chem. Phys.* **80**, 1625–1631, DOI: 10.1063/1.446862 (1984).
3. Kosloff, R. Quantum thermodynamics: A dynamical viewpoint. *Entropy* **15**, 2100–2128, DOI: 10.3390/e15062100 (2013).
4. Vinjanampathy, S. & Anders, J. Quantum thermodynamics. *Contemp. Phys.* **57**, 545–579, DOI: 10.1080/00107514.2016.1201896 (2016).
5. Binder, F., Correa, L. A., Gogolin, C., Anders, J. & Adesso, G. (eds.) *Thermodynamics in the Quantum Regime: Fundamental Aspects and New Directions*, vol. 195 of *Fundamental Theories of Physics* (Springer, Cham, 2018).
6. Goold, J., Huber, M., Riera, A., del Rio, L. & Skrzypczyk, P. The role of quantum information in thermodynamics—a topical review. *J. Phys. A: Math. Theor.* **49**, 143001, DOI: 10.1088/1751-8113/49/14/143001 (2016).
7. Alicki, R. & Lendi, K. *Quantum Dynamical Semigroups and Applications*, vol. 717 of *Lecture Notes in Physics* (Springer, Berlin, Heidelberg, 2007).
8. Ng, N. H. Y., Mančinska, L., Cirstoiu, C., Eisert, J. & Wehner, S. Limits to catalysis in quantum thermodynamics. *New J. Phys.* **17**, 085004, DOI: 10.1088/1367-2630/17/8/085004 (2015).
9. Cleri, F. Quantum computers, quantum computing, and quantum thermodynamics. *Front. Quantum Sci. Technol.* **3**, 1422257, DOI: 10.3389/frqst.2024.1422257 (2024).
10. Ptaszyński, K. & Esposito, M. Thermodynamics of quantum information flows. *Phys. Rev. Lett.* **122**, 150603, DOI: 10.1103/PhysRevLett.122.150603 (2019).
11. Faist, P., Berta, M. & Brandão, F. G. S. L. Thermodynamic implementations of quantum processes. *Commun. Math. Phys.* **384**, 1709–1750, DOI: 10.1007/s00220-021-04107-w (2021).
12. Sachdev, S. Quantum phase transitions. *Phys. World* **12**, 33, DOI: 10.1088/2058-7058/12/4/23 (1999).
13. Quan, H. T., xi Liu, Y., Sun, C. P. & Nori, F. Quantum thermodynamic cycles and quantum heat engines. *Phys. Rev. E* **76**, 031105, DOI: 10.1103/PhysRevE.76.031105 (2007).
14. Lieb, E., Schultz, T. & Mattis, D. Two soluble models of an antiferromagnetic chain. *Annals Phys.* **16**, 407–466 (1961).
15. Barouch, E. & McCoy, B. M. Statistical mechanics of the XY model. II. *Phys. Rev. A* **3**, 786–804 (1971).
16. Sachdev, S. *Quantum Phase Transitions* (Cambridge University Press, 2011), 2nd edn.
17. Dziarmaga, J. Dynamics of a quantum phase transition and relaxation to a steady state. *Adv. Phys.* **59**, 1063–1189, DOI: 10.1080/00018732.2010.514702 (2010).
18. Polkovnikov, A., Sengupta, K., Silva, A. & Vengalattore, M. Colloquium: Nonequilibrium dynamics of closed interacting quantum systems. *Rev. Mod. Phys.* **83**, 863–883 (2011).
19. B. S, R., Mukherjee, V., Divakaran, U. & del Campo, A. Universal finite-time thermodynamics of many-body quantum machines from Kibble-Zurek scaling. *Phys. Rev. Res.* **2**, 043247, DOI: 10.1103/PhysRevResearch.2.043247 (2020).
20. Denzler, T., Santos, J. F. G., Lutz, E. & Serra, R. M. Nonequilibrium fluctuations of a quantum heat engine. *Quantum Sci. Technol.* **9**, 045017, DOI: 10.1088/2058-9565/ad6287 (2024).
21. Campisi, M. & Fazio, R. The power of a critical heat engine. *Nat. Commun.* **7**, 11895, DOI: 10.1038/ncomms11895 (2016).
22. Ma, Y.-H., Su, S.-H. & Sun, C.-P. Quantum thermodynamic cycle with quantum phase transition. *Phys. Rev. E* **96**, 022143, DOI: 10.1103/PhysRevE.96.022143 (2017).
23. Piccitto, G., Campisi, M. & Rossini, D. The ising critical quantum Otto engine. *New J. Phys.* **24**, 103023, DOI: 10.1088/1367-2630/ac963b (2022).